Radiation Pressure effects on ion Acceleration on the GEMINI laser

Contact: m.borghesi@qub.ac.uk

M.Borghesi, R. Prasad, S. Ter- Avetisyan, D. Doria, K.E. Quinn, L. Romagnani, M. Zepf
School of Mathematics and Physics, Queen's University Belfast, Belfast, UK
D.C. Carroll, O. Tresca, P. McKenna
SUPA, Department of Physics, University of Strathclyde, Glasgow, UK

P.S. Foster, C.M. Brenner, P. Gallegos,J.S. Green, A. P. L. Robinson, D. Neely
CLF, Rutherford Appleton Laboratory, STFC, Oxfordshire, UK

N. Dover, C.A.J. Palmer, M.J.V. Streeter, J. Schreiber, Z. Najmudin
The Blackett Laboratory, Imperial College, London, UK

Introduction:

The dominant mechanism in most laser-driven proton acceleration experiments so far, the so-called Target Normal Sheath Acceleration (TNSA) [1], relies on the laser energy first being converted into a beam of relativistic electrons on a target foil. When these electrons exit the rear of the foil, a sheath field in excess of 10^{12}V/m is formed, which accelerates surface ions. Despite some advantageous properties [2], several factors limit the prospects of TNSA-driven beams for future applications: a relatively slow energy scaling, a large energy spread, and a low laser-to-ion energy conversion efficiency into the spectral region near the maximum energy .

Radiation Pressure Acceleration is a separate mechanism [3-6] where a large accelerating field arises by charge separation sustained by the ponderomotive pressure of intense laser radiation. Radiation pressure effects have previously been recognised as important to the dynamics of the interaction of the laser pulse with a solid target [7], leading to rapid deformation of the plasma surface and ions being driven into the target via the *hole-boring* process . In the limit of sufficiently thin foils (i.e. where the holeboring extends to the rear target surface during the laser pulse) the laser accelerates all the ions in the laser path and the acceleration scales as if the foil were being pushed as a whole, in the so-called 'light-sail' regime. Momentum balance considerations show that the change in the momentum p of the entire foil must balance the laser momentum resulting in

$$\frac{dp}{dt} \propto \frac{2I}{\sigma}$$

i.e. the acceleration becomes more effective as the areal mass density σ is reduced , as long as the target remains opaque to the laser.

The ion energy in the light-sail regime thus scales as the square of the laser intensity - or somewhat more slowly once relativistic effects have been taken into account [8]. This rapid scaling suggests that in ultraintense interaction regimes RPA should become the dominant effect on ion dynamics in laser interactions with thin solid foils. At present intensities ($I< 10^{21}$ W/cm^2), radiation pressure effects are difficult to detect. Linearly polarized pulses, normally used in interaction experiments, lead to strong electron heating via the oscillating component of the laser's ponderomotive force [8], and to a dominance of TNSA acceleration, which masks RPA effects. The use of circularly polarized light has been suggested as a way to isolate radiation pressure effects at present intensities [4,9]. In this case, the magnitude of the laser fields is constant during an optical cycle leading to a non-oscillating, quasi-static ponderomotive push on the target electrons. A large space-charge field arises from the electrons' separation from their parent ions, while electron heating is strongly reduced [9]. However, even with circular polarization, TNSA can arise at the edge of the laser focus as the target is deformed under the spatially non-uniform pressure drive associated to typical Gaussian or Airy-type focal spot profiles. This is due to the appearance of a small oscillating electric field component normal to the surface which can accelerate relativistic electrons and drive an (albeit weaker) TNSA foil expansion [10]. For this reason, 2D PIC simulations suggest that, in realistic irradiation conditions, transition into the light-sail regime requires a stronger drive ($I>10^{20}$Wcm^{-2}) [4]. A further point to be taken into account is that, due to surface contaminants, most real targets consist of at least two species, which affects the acceleration dynamics [4,6,11].

We report on an experiment performed by the LIBRA consortium [12] on the ASTRA-GEMINI facility, in which we aimed to detect radiation pressure effects on ion acceleration from ultrathin foils by using ultraintense, high contrast, circularly polarized laser pulses.

Experimental Methods:

The ASTRA GEMINI laser is a Ti:Saphhire based laser which delivered up to 15J in 40-50fs during our experiment. The intensity contrast nanoseconds before the peak of the pulse was enhanced by a factor of ~10^4 using a double plasma mirror system [13] with 50-60% reflectivity. This resulted in a peak/prepulse contrast of >10^{12}:1 at ns timescales and of 10^8:1 at 4ps from the peak of the pulse. The laser was focused onto the targets at normal incidence using an f/2 off-axis parabolic mirror resulting in a 2.5μm FWHM focal spot containing approximately 40% of the laser energy in the

FWHM. Resultant peak intensities were in the range 1-5 10^{20} Wcm^{-2}. The targets were amorphous carbon foils with thicknesses of 10-100nm. These foils have a hydrocarbon contamination a few monolayers in thickness, which is the origin of the protons observed in our spectra. The thicknesses of the foils are as quoted by the manufacturer and do not include an estimate for the hydrocarbon contamination layer that rapidly forms in all conditions other than ultra-high vacuum. A typical estimate of the contamination layer thickness is on the nm scale. The primary diagnostic for the recording of ion spectra was a Thomson parabola spectrometer, which employs parallel electric and magnetic fields to achieve energy dispersion and species separation (B=0.8T, E_{max}=10kVcm^{1}). The particles were detected using a calibrated microchannel plate detector (MCP) [14].

Circular polarisation was used for all shots discussed in this report in order to suppress electron heating and TNSA. In order to aid the interpretation of the data, 2D Particle-in-Cell simulations were carried out using the OSIRIS code [15]. A simulation box of 20 x 30 microns was used with a cell size of 2.5nm. The target is a 25nm foil with a mass density of 1gcm^{-3}. In terms of composition, it consists of carbon at a density of 50n_{crit} and a homogeneous proton contaminant population at 10 n_{crit}. A circularly polarized laser pulse is normally incident on the foil from the left. The pulse has a Gaussian temporal and transverse spatial profile with a spot size of 2.5μm and FWHM of 32fs. The amplitude of the pulse, in terms of normalized vector potential a_0 was 10 in the simulations of figure 2 (a_0=eA/m_ec, where A is the vector potential of the laser field, e and m_e are charge and mass of the electron. In practical units, a_0= (7.3 10^{-19} I λ2)$^{0.5}$, where the laser intensity I and the wavelength λ are expressed in W/cm^2 and μm, respectively).

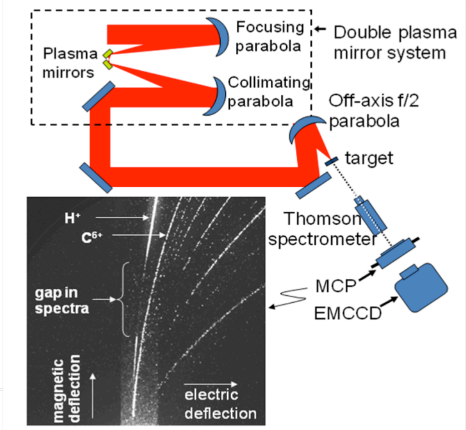

Figure 1: Experimental layout and sample of raw data. The plasma mirrors are implemented separately from the ion acceleration experiment). The raw data shows a distinct high-energy proton peak. The dominant H^+ and C^{6+} spectral tracks are indicated by arrows.

Results and Discussion:

Figures 1 and 2 show representative raw data and spectra taken at peak intensity with circular polarization. The proton spectra show peaks (~5 MeV in 2(a) and 9 MeV in 2(b)). In 2(b) the spectrum extends to ~20 MeV, and also displays a separate low energy component, with exponentially decreasing numbers up to a ~ 4 MeV cut-off. Comparison with 2D PIC simulations (figure 2 c) shows substantial agreement with the experimentally measured spectra and allows identifying the different spectral components. The low energy component is associated with TNSA-type acceleration taking place at large radii driven by hot-electrons generated at the outer edges of the focal spot (at a distance of several time the FWHM radius from its centre), while the peaked component of the spectrum is due to RPA at the centre of the spot.

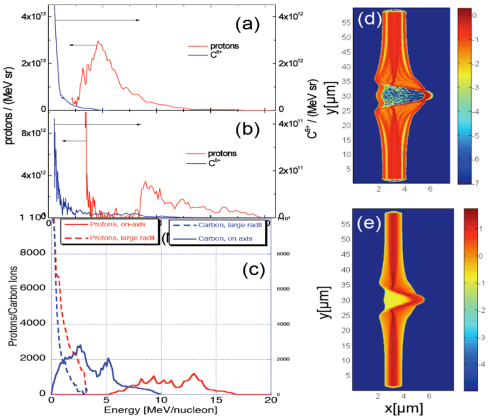

Figure 2: Comparison of experimental data and PIC simulations**. a,b** The spectra shown were recorded with circularly polarized pulses normally incident on 25nm carbon foils. Both profiles show a clear peak in the proton spectrum (red line). Such peaks were only clearly observed for circular polarisation. The inferred intensities are 1.6 10^{20}Wcm^{-2} and 2 10^{20}Wcm^{-2} respectively. **c** Simulated spectra at the end of the laser pulse for carbon ions and protons for an intensity of 2 10^{20} Wcm^{-2}. The contributions from the central part of the laser spot only (RPA component, solid line) and the region outside the focal spot (TNSA component, dashed line) are shown separately. The combined carbon and proton spectra fit well with the observed spectra in **b**. The corresponding proton and carbon 2D density plots are shown in **d**,**e**. The laser is incident from the left, centered at y=10µm and the initial foil position is at x=3µm. Comparison of d and e shows that, on axis, the protons travel ahead of the Carbon ions. The colour bars are in units of log(n/n_c), where n is the electron density and n_c is the critical density for the incident radiation.

These distinct regions of foil acceleration are identifiable in the simulated 2D density plots shown in figure 2d and e. The foil expansion far from the laser focal region is quite uniform both in the forward and backward directions and contains the full range of energies from 0 to the local maximum energy. In the central region, where the laser pressure is high enough to drive RPA there is a clear gap between the initial foil position and the accelerated foil where no protons/ions are present, corresponding to a peaked spectrum. No distinct RPA peak is visible in the carbon spectra due to a partial overlap with the low energy TNSA feature. However, close comparison of figure 2b and c indicates that the shoulder in the carbon spectrum extending to higher energies originates from RPA at the focal spot centre, while the rapid drop at energies below 2 MeV/u is due to TNSA at the outer edges of the spot.

The spectral features observed are consistent with the detailed two-species dynamics of RPA acceleration in the light-sail regime as observed in PIC simulations [2, 4, 20]. While the force on the electrons is constant, the ions are repeatedly accelerated in the quasi-static potential gradient (effectively a self-organized double layer [27]) set-up by the laser driven separation between electrons and ions. The higher charge-to-mass ratio of protons results in the protons gaining slightly higher velocity than the C ions in the moving electric field spike, and propagating ahead of the RPA-driven Carbons. Simulations indicate that the minimum proton velocity should typically correspond to the maximum C^{6+} velocity [2, 4, 20], a distinctive feature of the ion spectra obtained in our experiment. By contrast, the dynamics in the *hole-boring* regime are very different [28] and should result in almost identical energies for C^{6+} and protons. The spectral peak features were not observed when decreasing significantly the intensity or increasing the target thickness above 25 nm, conditions which resulted in lower proton energies and continuous spectra. In all these cases, the laser intensity was not sufficient to enter the light-sail regime, and the spectral features were determined by TNSA (thicker foils typically require higher intensities in order to achieve light sail [16].

The maximum energies observed in our experiments with circular polarisation at normal incidence are ~ 140MeV Carbon ions and ~ 20MeV protons respectively.

Conclusions

Employing circularly polarized, ultra-short (50 fs), high-contrast, high-intensity pulses, we have observed novel features in the ion spectra, namely a narrow band peak in the proton spectrum correlating with the end energy of the corresponding Carbon spectrum. The scaling of the peaks (not discussed here), their dependence on polarization and target thickness, and comparison with PIC simulation results, suggest that the spectral feature correspond to the onset of *light sail* Radiation pressure acceleration.

Acknowledgements:

This work was funded by EPSRC grants EP/E035728/1(LIBRA consortium), EP/F021968/1 and EP/C003586/1, and by STFC Facility access. We acknowledge the support and contribution of the Target Preparation Laboratory, ASTRA laser staff and the Engineering workshop at CLF, RAL.

References:

1. R.A. Snavely *et al,* Phys. Rev. Lett. **85**, 2945 (2000); S.C. Wilks *et al.,* Phys. Plasmas **8**, 542 (2000)
2. M. Borghesi *et al.,* Fus. Sci Tech, **49**, 412 (2006)
3. T. Ezirkepov, *et al., Phys. Rev. Lett.* **92**, 175003 (2004)
4. A. P. L. Robinson *et al., New J. Phys.* **10**, 013021 (2008).
5. B. Qiao *et al., Phys. Rev. Lett.* **102**, 145002 (2009)
6. A. Macchi *et al.,Phys. Rev. Lett.* **103**, 085003 (2009)
7. S.C. Wilks *et al., Phys. Rev. Lett.* **69**, 1383-1386 (1992)
8. A.P.L. Robinson *et al., Plasma Physics and Controlled Fusion* **51**, 024004 (2009)
9. A. Macchi *et al., Phys. Rev. Lett.* **94**, 165003(2005)
10. M. Chen et al., Phys. Rev. Lett. 103 024801 (2009)
11. O. Klimo *et al.,* Phys. Rev. S.T.-Accelerators and Beams, **11**, 031301 (2008)
12. http://www.qub.ac.uk/sites/LIBRA
13. B. Dromey *et al., Rev. Sci. Inst.* **75,** 645-649 (2004)
14. R. Prasad et al., Nucl. Instr. and Meth. A (2010), doi:10.1016/j.nima.2010.02.078

Ion acceleration from foil targets in the ultraintense ultrahigh contrast regime.

Contact *olivier.tresca@strath.ac.uk*

O Tresca,[1] D C Carroll,[1] R Prasad,[2] L Romagnani,[2] P S Foster,[3,2] P Gallegos,[1,3] S Ter-Avetisyan,[2] J S Green,[3] M J V Streeter,[3,4] N P Dover,[4] C A J Palmer,[4] C M Brenner,[1,3] F H Cameron,[3] K E Quinn,[2] J Schreiber,[4] A P L Robinson,[3] T Baeva,[3] M N Quinn,[1] X H Yuan,[1] Z Najmudin,[4] M Zepf,[2] D Neely,[3,1] M Borghesi,[2] and P McKenna,[1]

[1] SUPA Department of Physics, University of Strathclyde, Glasgow G4 0NG, UK

[2] School of Mathematics and Physics, Queen's University Belfast, Belfast BT7 1NN, UK

[3] Central Laser Facility, STFC Rutherford Appleton Laboratory, Didcot, Oxfordshire OX11 0QX, UK

[4] The Blackett Laboratory, Imperial College London, London SW7 2AZ, UK

Introduction

The acceleration of ions from the interaction of intense laser pulses with thin solid targets has generated a great deal of experimental and theoretical interest since the first multi-MeV energy ion beams were first produced in 2000 [1-6]. Those beams have shown highly desirable properties such as high brightness and low transverse and longitudinal emittance [7] with potential applications in inertial confinement fusion [8], nuclear physics [9] and medicine [10-11]. The main mechanism responsible for the acceleration of ions in laser conditions that are available today is the so called Target Normal Sheath Acceleration (TNSA), where ions from the surfaces of the target are accelerated by an electrostatic sheath field of a few TV/m. This sheath field is generated by the hot electron population, resulting from the coupling of the laser energy into the target. These electrons propagate from the front surface of the target and exit at the rear surface where they set up a large electrostatic field caused by the charge separation between the ions on the rear surface and the electrons attempting to escape from the target. The strength of the sheath field is such that the majority of the electrons are pulled back into the target. In this scheme ions with a high charge to mass ratio are preferentially accelerated, namely protons. The TNSA mechanism is the dominant ion acceleration mechanism for laser intensities ranging form 10^{18} to 10^{20} Wcm^{-2} and for targets thicker than 50nm [12]. For thinner targets and higher laser intensities, new acceleration mechanisms prevail such as Coulomb explosion [13] or radiation pressure acceleration (RPA) [14-15]. Such schemes are predicted to give rise to peaked energy spectrum for the ions, with a maximum energy in the hundreds of MeV.

In this report we will report on recent experimental results obtained with the Astra-Gemini laser during the LIBRA campaign in march-July 2009 during which the acceleration of carbon ion by the TNSA mechanism has been investigated, especially the effect of the laser incidence angle. Experimental results are discussed with reference to 1D PIC simulations.

The experiment

The Astra-Gemini laser delivers pulses with duration, τ_L, of 50fs, energy, E_L, up to 12J at a wavelength, λ_L, of 800nm. A double plasma mirror system was used to enhance the contrast up to ~10^{10} on the ps scale. The targets were irradiated under two different incident angles, 35° from target normal and 0° to the target normal. The laser pulses were focused using an *f*/2 OAP onto 1.25 μm radius focal spot in the 0° configuration with 35% of the energy in the central spot. The calculated intensity on target was 7×10^{20} Wcm^{-2}.

A wide range of target materials were used during the experiment including plain foils of C, $C_{10}H_{10}O_4$ (CHO, mylar), C_3H_6 (CH, polypropylene), Au and Al as well as layered Au-CH targets. The target thickness, L, was varied between 50nm and 10μm.

The ion beam properties were measured using two Thomson parabola spectrometers, positioned along the target normal direction for the two incidence angles as shown in figure 1.

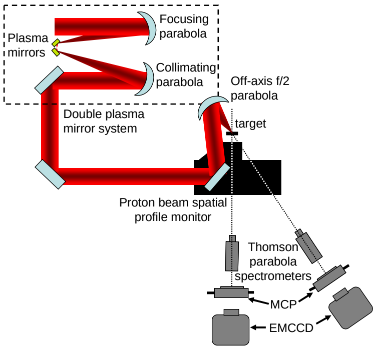

Figure 1: Schematic of the experimental setup.

A combination of Micro Channel Plate detectors and intensified Andor CCD cameras were used to record the dispersed ions. The arrangement was absolutely calibrated using slotted CR39 track detector [16].

Effect of laser incident angle on ion acceleration

Our attention was primarily focused on the acceleration of carbon ions for different target materials and thicknesses at two fixed incident angles. As shown in figure 2, clear changes in the spectra are visible when the laser incident angle changes from 35° to 0°. The number of accelerated ions as well as the maximum energy increases when the angle of incidence is changed from oblique to normal.

As shown in figure 4, this increase in maximum ion energy is independent of target thickness as well as target material. An increase by a factor ~1.3 is observed throughout the whole thickness range, over 2 orders of magnitude.

This result is in stark contrast with previous work by Ceccotti et al [17] where the effect of laser polarisation, s or p, on the acceleration of protons is investigated. They reported that for laser pulses of 65fs with intensities of 5×10^{18} Wcm^{-2} and a contrast of 10^{10} the higher proton energy is achieved using p-polarised pulses at oblique incidence where the Brunel absorption (vacuum heating) effect [18] and the collisionless absorption mechanism [19] efficiently transfer laser energy into the target. In the case of an s-polarised laser pulse, because the laser electric field is in the plane of the target, the aforementioned absorption mechanisms have their efficiency drastically reduced, therefore diminishing the maximum proton energy.

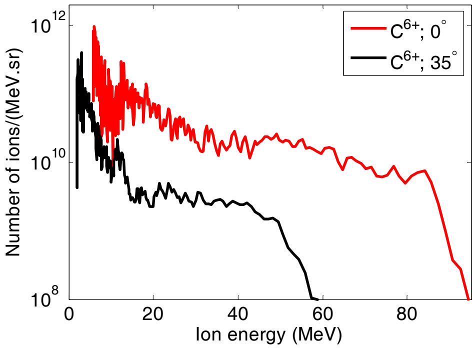

Figure 2: Experimental C^{6+} spectra obtained for two different incidence angle, 0^o (in red) and 35^o (in black).

In our case the laser pulse polarisation was kept constant (p-polarised) and only the incidence angle was changed. The p-polarised pulse at normal incidence is equivalent to an s-polarised pulse at normal incidence, making a comparison with Ceccotti *et al* work possible. The fact that, at higher intensities, we observe a more efficient coupling of the laser energy into the ions, which cannot be explained by the change in the focal spot size, lead us to believe that a new angle dependent laser absorption mechanism is at play.

To have a better understanding of the absorption mechanism involved in our experiment we conducted a series of 1D and 2D PIC simulations for both incident angles.

The 1D simulations were done using a modified version of the code used in [20]. A box of 25000 cells each with a size of 2nm and containing 200 particles was simulated. The target consists of two layers, one heavier ion substrate with a Z equals to 1 and a mass three times that of a proton, and a thin proton layer on the rear of the target. Both layers have a density of 90 nc. A laser pulse duration of 50fs at a wavelength of 800nm and an a_0 of 18 (equivalent to $7\text{x}10^{20}\text{Wcm}^{-2}$) was used.

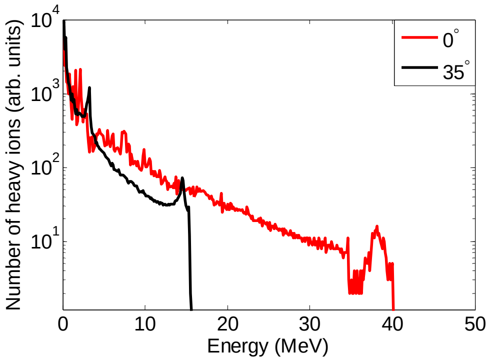

Figure 3: 1D PIC simulation result showing the energy distribution for the heavy ion population at two different incident angles, 0^o (in red) and 35^o (in black).

The 1D simulation results, displayed in figure 3, show a clear increase in maximum ion energy when the laser incident angle is changed from 35^o to 0^o. The increase in energy for the 1D case is found to be ~2.6, which is slightly higher than the increase measured in the experimental data.

Effects of target properties on ion acceleration

The effect of the target properties, thickness and material, was also investigated. Figure 4 shows a summary of the measurements obtained using Al, C and CHO foils. Each point represents the average maximum C^{6+} ion energy for 3 to 4 laser shots on each target at the different thicknesses.

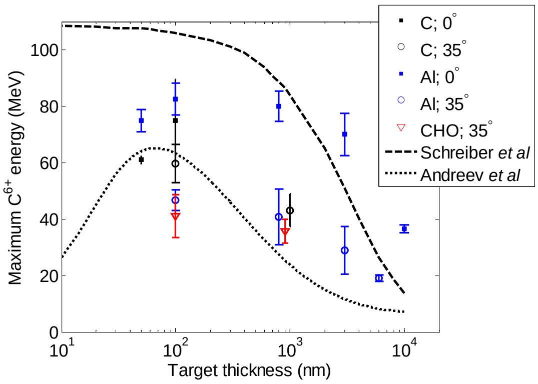

Figure 4: Average of the maximum C^{6+} ion energy over multiple shots as a function of target thickness for different materials. The errors bars represent the standard deviation of the maximum energy.

A scaling of the maximum ion energy with target thickness, and independent from target material, is observed. The increasing rate of the maximum energy is very similar to the one reported in Neely *et al* [21] for protons. An increase of a factor 2 in the maximum ion energy is observed when the target thickness is reduced by two orders of magnitude This can be explained by the fact that the transverse spreading of the electron beam propagating through the target is increased as the target thickness increases and the effects of refluxing electrons are reduced [22], therefore limiting the acceleration of the ion by the TNSA mechanism.

Two analytical models were applied to the data in order to investigate the expected scaling of the maximum ion energy; the model presented by Andreev *et al* [23] and the model proposed by Schreiber *et al* [24]. Both models predict an increase in maximum energy with decreasing target thickness down to 100nm, in qualitative agreement with the experimental data. Andreev *et al* model predicts an optimal thickness around 80nm for our experimental parameters. On the other hand, the Schreiber *et al* model shows saturation of the maximum energy for thicknesses of ~100nm. Experimentally, we observe changes in the energy spectra for targets below 100 nm, suggesting that the ion acceleration mechanism is not purely TNSA.

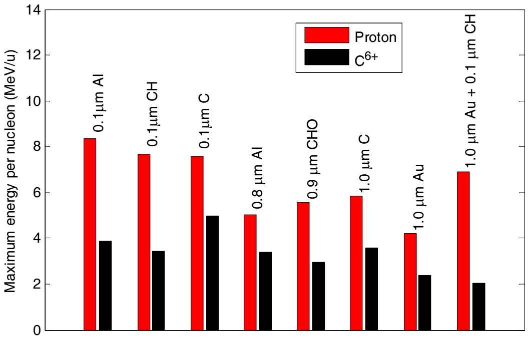

Figure 5: Maximum protons and C^{6+} ion energies for different target composition and thicknesses.

Figure 5 displays the average maximum proton and C^{6+} ion energy for different target materials at different thicknesses. This allows us to compare the effect of the presence of carbon in the target as a bulk material (C, CHO and CH targets), an uncontrolled surface contaminant layer (Al and Au) or a controlled deposited layer (Au-CH).

In the case of the C, CH and CHO targets we observed that the composition of the target does not affect the maximum proton energy significantly for a given thickness. However, in the case of C^{6+} the acceleration is more efficient for the pure C target.

This can be explained by the screening effect due to the presence of hydrogen in the CH and CHO targets. As for the controlled layer target (Au-CH), the addition of hydrogen in the accelerating field enhances the production of protons. A small decrease in the carbon ion energy is observed, further confirming that the presence of protons limits the acceleration of heavier ions.

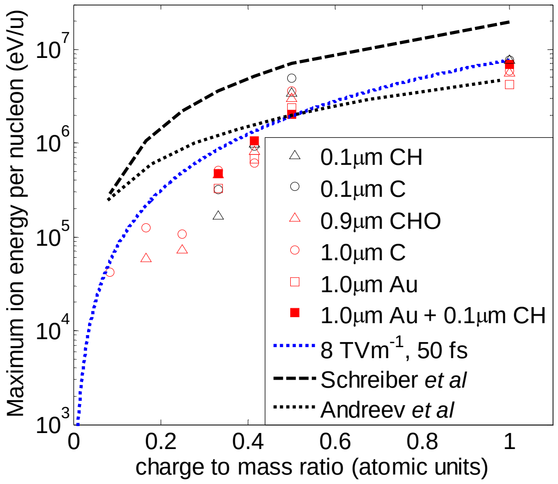

Figure 6: Maximum ion energy as a function of the ion charge to mass ratio

Figure 6 shows the variation of the maximum ion energy as a function of the charge to mass ratio. A clear increase, by a factor of 2, is observed over the range *q/m*=0.1-0.5. The analytical models by Schreiber *et al* (dashed black*)* and Andreev *et al* (dotted black) are also represented. The Schreiber *et al* model is in good agreement with the experimental trend but overestimates the measured energies, while the Andreev *et al* model gives energies closest to the highest measured but does not follow the trend as well. Both models fail to reproduce the lower charge state energies; shielding effects that are not taken into accounts in the models may be responsible for this. A simple model (dotted blue) where the ions are assumed to be accelerated by a simple electrostatic field and the free parameter is the electric field strength, the estimated energies for 8TV/m field is shown. This simple model reproduces the experimental data surprisingly well.

Conclusions

We have conducted an experiment using the Astra-Gemini laser in 2009 during which we investigated the effect of the laser incident angle on the ion acceleration in the TNSA regime. We observed for the first time that at the laser intensity available, $7\text{x}10^{20}$ Wcm^{-2}, the coupling of the laser energy into the ions is greater at normal incidence than at oblique incidence. This observation is inconsistent with previous work by Ceccotti *et al* [17] intensity. The increase in maximum ion energy can not be explained by the small difference in laser intensity at the two angles, therefore suggesting that a new angular dependent absorption process may occur at these higher laser contrasts and intensities.

1D PIC simulations were performed to investigate further this possible new absorption mechanism. The experimental data were well reproduced by the simulations. 2D simulations were also conducted to explore the effect of the incident angle on the electron population. Preliminary analysis suggests that higher energy fast electrons are produced in the normal incidence case.

We also found that with the laser parameters available during the experiment the maximum ion energy increases with decreasing target thickness down to 100nm independently from target material for the TNSA mechanism. For thinner targets, changes in the energy spectra were observed suggesting that the acceleration mechanism is not purely TNSA.

The investigation of the effects of the target material on the acceleration of carbon ions showed that the highest energy carbons are obtained with targets containing carbon but no hydrogen as a bulk material. The presence of hydrogen, throughout the target or on the surface reduces the energy coupling to the carbon ions. By contrast, it is found that the acceleration of protons can be enhanced for a high Z material when a hydrogen rich layer is deposited on the back surface.

An increase in the maximum ion energy with increasing *q/m* ratio was observed and analytical models were applied to the data. It has been found that a simple electrostatic acceleration model gives a reasonable fit to the data as a function of *q/m*. Unconsidered screening effects, in the models, of the lower ion charge states may explain the difference between the models and the data for these ions. For further reading please see [25].

Acknowledgements

We acknowledge the expert support of the staff at the Central Laser Facility. This work was supported by the UK Engineering and Physical Science Research Council (grant numbers EP/E035728/1 and EP/E048668/1) and the LIBRA consortium. Computing resources were provided by the STFC's e-Science facility.

References

1. Clark E L *et al* 2000, *Phys Rev Lett* **84** 670-3
2. Snavely R A *et al* 2000, *Phys Rev Lett* **85** 2945-8
3. Hegelich M *et al* 2002, *Phys Rev Lett* **89** 085002
4. Borghesi M *et al* 2006, *Fusion Sci Technol* **49** 412-439
5. Robson L. *et al* 2007, *Nat. Phys* **3** 58-62
6. P. Mckenna *et al* 2003, *Appl. Phys. Lett* **83** 14
7. Cowan *et al* 2004, *Phys Rev Lett* **92** 204801
8. Roth M, *et al*. 2001 *Phys Rev Lett* **86** 436-9
9. McKenna P, *et al*. 2003 *Phys Rev Lett* **91** 075006
10. Bulanov S V, *et al* 2002 *Phys Lett A* **299** 240-7
11. Malka V, *et al*. 2004 *Medical Physics* **31** 1587-92
12. Henig A *et al* 2009, *Phys Rev Lett* **103** 045002
13. Bulanov S S *et al* 2008, *Phys Rev E* **78** 026412
14. Henig A *et al* 2009, *Phys Rev Lett* **103** 245003
15. Robinson *et al* 2009, *Plasma Phys. Control. Fusion* **51** 024004
16. R. Prasad *et al*, 2010, *Nucl. Instr.and Meth. A* doi: 10.1016/j.nima.2010.02.078
17. Ceccotti T *et al* 2007, *Phys Rev Lett* **99** 185002
18. Brunel F 1987, *Phys Rev Lett* **59** 52-5
19. Gibbon P 1994, *Phys Rev Lett* **73** 664-7
20. Robinson A P L *et al* 2008, *New J Phys* **10** 013021
21. Neely D *et al* 2006, *Appl Phys Lett* **89** 021502
22. Sentoku Y *et al* 2003, *Phys. Plasmas* **10** 2009–15
23. Andreev A *et al* 2008, *Phys Rev Lett* **101** 155002
24. Schreiber J *et al* 2006, *Phys Rev Lett* **97** 045005
25. Carroll D C *et al* 2010, *New J Phys* **12** 045020

Characterisation of debris emission from thick targets on Astra-Gemini

Contact *david.carroll@strath.ac.uk*

D C Carroll,[1] R J Clarke,[2] P S Foster,[2,3] J S Green,[2] C Spindloe,[2] M J V Streeter,[2,4] O Tresca,[1] D Neely,[2,1] and P McKenna,[1]

[1] SUPA Department of Physics, University of Strathclyde, Glasgow G4 0NG, UK

[2] Central Laser Facility, STFC Rutherford Appleton Laboratory, Didcot, Oxfordshire OX11 0QX, UK

[3] School of Mathematics and Physics, Queen’s University Belfast, Belfast BT7 1NN, UK

[4] The Blackett Laboratory, Imperial College London, London SW7 2AZ, UK

Introduction

The issue of debris from solid targets has been a concern since the advent of higher power lasers where protective barriers, such as glass pellicles [1], are used to protect optics. However with high repetition rate high power laser systems now coming online or in the design stages [2-4] the issue of debris is becoming more significant [5] as the accumulation of damage or surface coating is more rapid.

We report we report on debris characterisation measurements made during the radiation commissioning of the Astra-Gemini laser in early 2009. During the commissioning the distribution of debris from thick targets around the horizontal plane of the target was studied. Debris in this report is defined as to encompass all material leaving the target; liquid, vapour and solid (shrapnel).

Experimental setup

The Astra-Gemini laser delivers pulses with duration, τ_L, of 50fs, energy, E_L, up to 15J at a wavelength, λ_L, of 800nm. The laser incident angle onto target was 35^o relative to the target normal. The laser pulses were focused using an *f*/2 OAP onto 1.25 μm radius focal with 35% of the energy in the central spot. The calculated peak intensity on target is 6 x10^{21} Wcm^{-2}.

The targets used are 0.5 mm thick Tantalum (Ta), plastic (CH) and copper (Cu) and 50 μm thick gold (Au). The key diagnostics are four 127 mm square glass witness plates [ref RAL report] arrayed around the target as shown in figure 1. These glass plates accumulate debris on their front surfaces over shot sequences consisting of up to 30 shots.

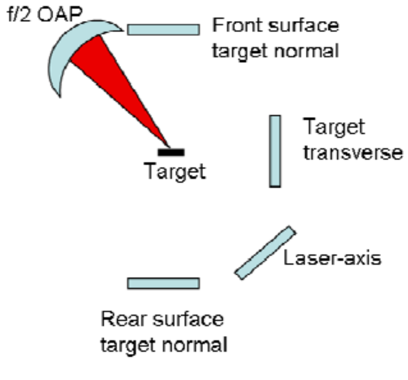

Figure 1: Schematic of the experimental setup.

These witness plates enable the study of three different debris types on surfaces. These are the build up of layers of debris coating on surfaces, macro sized pieces of debris embedded on surfaces and the damage caused by shrapnel like debris to the surfaces.

Table 1: Witness plate positions and distances, d, from target

Witness plate position	d (mm)	Solid angle (sr)
Front surface target normal axis	320	0.16
Target transverse	243	0.27
Laser axis target rear surface	230	0.30
Rear surface target normal	245	0.27

Debris from 500 μm thick targets

The debris generated from 500 μm thick targets of Ta, CH and Cu were accumulated on a single set of witness plates. There were in total 36 shots on CH, 48 shots on Cu and 47 shots on Ta. As these shots were primarily for the radiation commissioning there are shots within this total that were defocused, table 2 summarises this for each target, thought the majority were at best focus.

Table 2: Number of shots at different focus positions for the three materials used for 500 μm thick targets

	Estimated spot diameter (μm)							
Material	**3**	**10**	**20**	**30**	**50**	**100**	**250**	**500**
Cu	22	4	4	0	4	4	6	4
CH	12	4	4	0	4	4	4	3
Ta	38	1	3	1	2	0	0	0

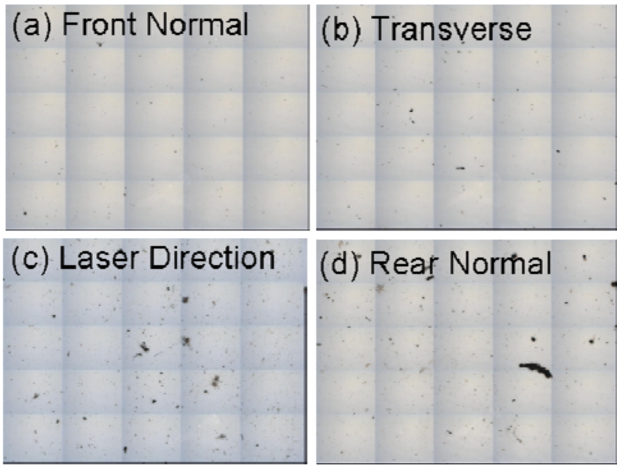

Figure 2: Scans of central area (15.9 x 11.9 mm) for each witness plate for 500 μm thick targets. (a) Front surface target normal, (b) target transverse, (c) laser axis and (d) rear surface target normal.

The debris distribution for this thickness of targets was found to favour emission in the laser-axis and rear surface target normal directions which showed the highest density of debris. This can be seen in Figure 2 which shows systematic scans of the central area for each of the witness plates, covering an area of 189 mm^2.

The debris particulates observed on the witness plates are large, typically around 400 μm. The debris is typically irregular in shape which is especially true for plastic. The plastic target was observed to produce the largest pieces of debris that stuck to the witness plate with sizes in the millimetre range (figure 2(d) shows one of these large pieces). For the metal targets if any such large pieces of debris were produced they were not captured by the witness plates. No large scale physical damage to the witness plates surfaces were observed

Debris from 50 μm thick targets

A second set of witness plates were used to capture the debris produced from the 50 μm Au targets shot during the radiation commissioning. The positions of the witness plates were kept the same as shown in figure 1 and listed in table 1. As before, multiple shots worth of debris were accumulated onto the witness plates, in this case the number of shots was 26. Within this were shots taken at different focus positions and are listed in table 3.

Table 3: Number of shots at different focus positions for the 50 μm thick Au targets

	Estimated spot diameter (μm)							
Material	**best**	**10**	**20**	**30**	**50**	**100**	**250**	**500**
Au	2	4	4	0	4	4	4	4

The distribution of debris from the thick 50 μm Au targets is found to be different to the case for the very thick 500 μm targets. For the thinner target the highest debris was found on the front and rear target normal witness plates and minimal amount on the laser axis and transverse plates. The largest debris particulates measured on the laser axis and transverse plates is 70 μm and 20 μm respectively. Scans of the central area for each of the witness plates are shown in figure 3.

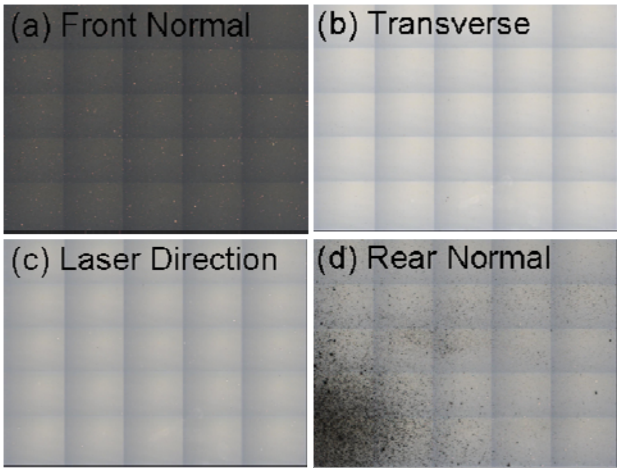

Figure 3: Scans of central area (15.9 x 11.9 mm) for each witness plate for 50 μm thick Au targets. (a) Front surface target normal (note this image is reflected rather than transmitted light to highlight gold debris), (b) target transverse, (c) laser axis and (d) rear surface target normal.

The debris on the front surface plate was found to be evenly distributed across the surface. The size of the debris particulates was found to be smaller in size than for the larger targets, largest debris size was found to be ~70 μm in size. The debris was also found be more uniform in shape, circular and flat on the glass surface. This is likely due to the Au material hitting the plate being molten droplets rather than solid shrapnel. The rear surface target normal plates

The rear surface target normal plate has a similar layer of evenly distributed debris across the surface as the front surface but also has an additional feature. This additional feature is an area of damage to the glass surface in a concentrated region around the actual target normal axis. This can be seen in the bottom left of figure 3(d). This indicates a beam like feature of highly destructive debris, shrapnel, coming from the target rear surface. This area of damage has distinct features, a central area where the pits in the glass are ~350 μm in size, two larger circular areas on damage above and below the central area which contain pits smaller in size of ~100 μm. The final feature is a line of damage from the central region going towards the laser axis with pits also around 100 μm in size. These features are shown in figure 4.

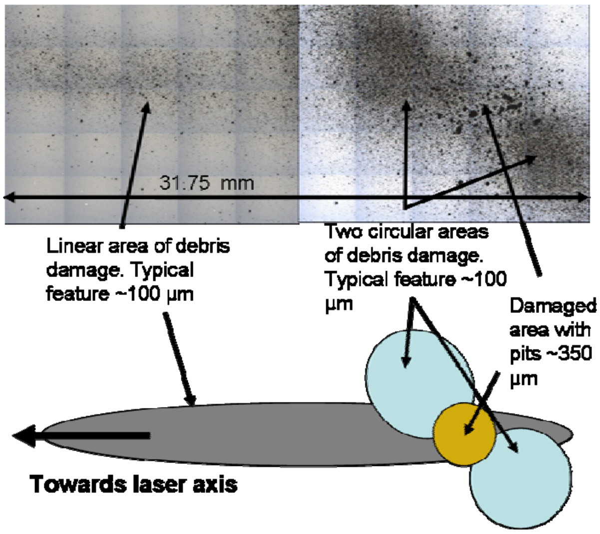

Figure 4: Debris damage to glass witness plate at the target normal rear surface position. The images at the top are scans of the damage to the plate surface and the bottom diagram is a schematic of features found in the damage distribution.

Debris production with the Phelix laser

Similar debris damage along the target normal rear surface axis was also observed on an experiment using the Phelix laser, based at the GSI facility in Germany.

The Phelix laser generates pulses that are of the order of a picosecond with energies in the 100 J range. The debris deposition along the target normal axis from 26 μm and 100 μm Au targets was obtained from the front Al layer of an RCF stack (50 mm x 50 mm) placed 40 mm behind the target, which acted as a witness sample.

It was observed that for 100 μm thick Au targets indents were formed in the Al layer. It was confirmed that these indents were being formed by Au debris from the target as Au shrapnel was found to be embedded in the 13 μm thick Al layer. This can be observed in figure 5(b).

When the 26 μm thick Au target was irradiated the results were drastically different in terms of debris damage. Instead of the indentation caused by debris impact it was found that a roughly radial symmetric discolouration of the Al layer had occurred, this can be seen in figure 5(a). This discoloration is purple in colour near the centre and gradually changes to a golden yellow at larger radii. This is an indication of heat damage to the Al layer and is likely due to non-shrapnel debris. Modelling is underway to determine the reasons for the change in size of debris particulates with target thickness.

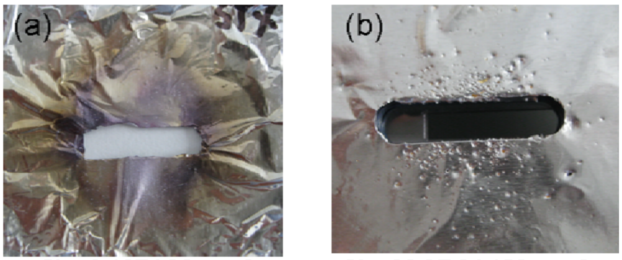

Shot6 167J 26 µm Au Shot22 87.9J 100 µm Au

Figure 5: Representative samples of the effects of debris on an Al witness foil placed along the target normal at the rear of: (a) 26 µm Au and (b) 100 µm Au targets. The thicker target produces shrapnel.

Conclusions

We have taken debris measurements with glass witness plates on Astra-Gemini during radiation commissioning and observed the effects that target thickness has on debris.

For 0.5 mm thick targets, large debris particulates were measured over a wide area with the highest density being measured in the laser axis and rear surface target normal directions. It was found that the debris particulates were not energetic enough to cause physical damage to the glass witness plates at a distance of ~25 cm. It was also found that the largest pieces of debris that stuck to the glass surfaces were from plastic targets.

For targets that were an order of magnitude thinner, 50 µm Au, the distribution of debris and it effects were found to have changed. It was weighted more towards the front and rear surfaces target normal axes. The debris at the front surface was found to form a coating on the glass witness plate consisting of circular discs, indicating the debris was molten or liquid when impacting on the plate. Similar debris coating at the rear surface was also found, but in addition severe damage to the glass surface was also observed. This indicated that the debris at the rear surface consisted of a mixture of shrapnel and liquid or molten pieces. Features were found in the distribution of damage to the glass surface consisting of a central area with largest damage, two surrounding hemi-spheres of lesser damage and a line of damage stretching towards the laser axis.

Similar damaging shrapnel was also observed on the Phelix laser for 100 µm thick Au targets. When the laser energy was increased and the target thickness decreased there was significantly less physical damage observed but thermal discolouration also occurred.

These initial observations indicate that the target thickness has a significant effect on the debris distribution and types of debris produced in the interaction environment. However, a more systematic study of debris is required to determine how changing laser and target parameters effect debris distribution and types. In particular the debris produced from ultra-thin targets, i.e. submicron, should be investigated as these targets are likely to have very different debris distributions and are the favoured target type for achieving the required ion beam properties for application [refs].

Acknowledgements

We acknowledge the expert support of the staff at the Central Laser Facility and the staff at the PHELIX laser facility at GSI, Darmstadt. This work was supported by the UK Engineering and Physical Science Research Council (grant numbers EP/E035728/1) and LaserLAB Europe. This work was performed in the context of the LIBRA grant.

References

1. http://optics.org/cws/product/P000001579
2. C.J. Hooker *et al*, *Commissioning the Astra Gemini Petawatt Ti:Sapphire Laser System*, in Conference on Lasers and Electro-Optics/Quantum Electronics and Laser Science Conference and Photonic Applications Systems Technologies, OSA Technical Digest (CD) (Optical Society of America, 2008), paper JThB2
3. http://www.hiper-laser.org/
4. http://www.extreme-light-infrastructure.eu/
5. J.E. Andrews *et al*, *Observations of debris and shrapnel plumes from PW driven solid targets*, Central Laser Facility, UK, annual report 2007/2008

High rep rate Thomson parabola-MCP assembly for multi-MeV ion spectroscopy

Contact: rprasad01@qub.ac.uk

R.Prasad, D. Doria, S. Ter-Avetisyan, K.E. Quinn, L. Romagnani, M. Zepf,
M. Borghesi,
School of Mathematics and Physics, Queen's University Belfast, Belfast, UK
D.C. Carroll, O. Tresca,
P. McKenna
SUPA, Department of Physics, University of Strathclyde, Glasgow, UK

C.M. Brenner, P.S. Foster, P. Gallegos, J.S. Green, A. P. L. Robinson, D. Neely
CLF, Rutherford Appleton Laboratory, STFC, Oxfordshire, UK

N. Dover, C.A.J. Palmer, M.J.V. Streeter, J. Schreiber, Z. Najmudin
The Blackett Laboratory, Imperial College, London, UK

Abstract

We report on the absolute calibration of a micro channel plate (MCP) detector, installed as detector in a Thomson parabola spectrometer. The calibration delivers the relation between a registered count numbers in the CCD camera (on which the MCP phosphor screen is imaged) as a result of the impact of an ion beam onto the MCP. The particle response of the whole detection system was evaluated by using laser accelerated ions with proton energies up to 3 MeV and carbon ion energies up to 16 MeV. In order to obtain an absolute measurement of the number of ions incident on the MCP detector, slotted CR-39 track detector was installed in front of the MCP. The signal registered on the MCP due to ions propagating through the CR-39 slots is compared to the number of particles counted on the adjacent CR-39 stripes after the etching. The calibration of the response of MCP has been extended to higher energy ions and protons on the basis of a simple model validated by comparison with the calibration data. This sensitive detection set-up makes it possible to measure in a single laser shot the ion spectrum in absolute terms.

1. Introduction

High power (100TW–1PW) laser systems are capable of delivering ultraintense (up to 10^{21}W/cm^2), ultrashort (40–50 fs) laser pulses at high repetition rate (e.g. Astra-GEMINI laser-one pulse in every 20s). Energetic ions/protons accelerated up to tens of MeV energies per nucleon have been observed experimentally during the interaction of these pulses with thin solid targets [1–3]. Efficient detection of these particles is most important for their potential applications. The Thomson parabola spectrometer is successfully used as a charged particle analyzer [4] for the quantitative analysis of ion beams emerging from the laser plasma. The deflection of charged particles in homogeneous magnetic and electric fields provides simultaneously their energy, momentum, and mass-to-charge ratio. The spectrometer becomes uniquely valuable, particularly for use on a single shot basis, if coupled to absolutely calibrated, fast response detectors, such as, e.g. microchannel plate (MCP) detector coupled to a phosphor screen. Having a single shot online diagnostic is very important also because current laser systems still suffer from shot-to-shot fluctuations of laser pulse parameters, such as energy, pulse duration, and pulse shape, which significantly modify the interaction conditions and, thereby, the particle acceleration processes. This paper will describe the calibration of a Thomson-MCP assembly which we employed in a recent laser-driven ion acceleration experiment. We will discuss the method employed, the relevant data analysis and a theoretical model for the MCP response which allows to extend the calibration data to higher energy ranges. Careful consideration is required in evaluating the response of the MCP, since in the arrangement employed different energy ions are incident on the MCP at different angles (unlike, for example, ions accelerated by linear accelerators), and this may affect the gain and secondary electron yield. For this reason, an in-situ calibration is important for a correct data analysis.

2. Method and calibration

In the experiment, thin planar foil targets were irradiated at 35^0 incidence by p-polarized laser pulses from the Astra-GEMINI laser system at the Rutherford Appleton Laboratory (RAL) with energy of up to 12J and pulse duration _50 fs. With an f/2 off-axis parabolic mirror, a maximum vacuum intensity of 5_10^{20} W/cm^2 was reached with a double plasma mirror system. The measurements of the energies of the ions emitted normal to the target were carried out with a Thomson parabola spectrometer schematically shown in Fig. 1. Typically, a magnetic field of about 0.4T and electric field of 8 kV/cm have been applied. The ions are detected by a Hamamatsu MCP (Model-AF2226-A093B) detector with a diameter of 77mm and bias angle 8^0 coupled to a phosphor screen (P-43) which is imaged with an objective onto the chip of a CCD camera. In order to calibrate the MCP we placed a slotted CR-39 track detector [5] in front of the MCP. With this arrangement the spectral parabolic traces of the ions will be partly detected on CR-39 while the parts, which pass through the gaps of the slotted CR-39, will appear on the phosphor screen of the MCP. The tracks on CR-39 produced after etching in a 6N NaOH solution at 70^0 C temperature of water bath for 3 hrs and the corresponding image from the phosphor screen of the MCP detector captured on CCD camera are shown in Fig.2(b) and (a), respectively. The number of protons and C^{6+} ions incident on each stripe on CR-39 were counted using an optical microscope where as a routine in Matlab was written to identify the ion species and their energies by fitting the different parabolic tracks from the image. This routine also provides the counts in each pixel of the CCD as a signal corresponding to the ions falling in that pixel region. We correlate the number of protons on each stripe to the adjacent CCD integrated counts belonging to the same parabolic trace. A complication encountered was that the portions of the traces projected on the CCD through the CR-39 gaps for the lower energy part of the spectrum appeared smaller than their counter part on CR-39. This was due to the thickness (1mm) of theCR-39, coupled to the relatively large deflection angle of the low energy ions, which resulted in part of the trace being blocked. Therefore we considered the counts per unit energy interval integrated across the width of the stripe on the CCD image and the corresponding integrated number of protons on CR-39. In order to correlate CCD counts to number of protons we then interpolated the signal of two consecutive trace sections on the CCD and compared the interpolated value with the counts of the interleaved section on the CR-39. Similarly, interpolation of two consecutive CR-39 trace sections and comparison with the interleaving CCD trace section was also carried out. In this way we obtained the ratio (counts/particle) as a function of energy which gives the response of the MCP to protons. In the same manner the response to C^{6+} ions has been calculated. Data obtained from the comparison of spectral images on MCP and CR- 39 is shown in Fig. 3 for protons and C^{6+} ions. Although the calibration data shown are for protons up to 3 MeV and for carbon ions up to 16 MeV energies, the MCP response to higher energy ions was considered and a theoretical model has been proposed.

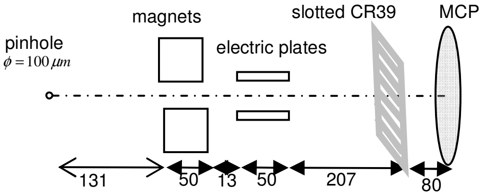

Fig.1 Schematic arrangement of the Thomson parabola spectrometer to detect the ions using the MCP detector coupled to the phosphor screen and CR-39 detector simultaneously (Distances in mm).

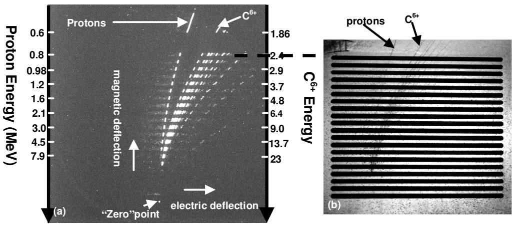

Fig.2 An image from the (a) MCP-phosphor screen and (b) CR-39 track detector of an emitted ion spectrum from 0.8 μm carbon foil target taken from a single laser shot in the target normal direction with the Thomson spectrometer. Here the CR-39 track detector was installed in front of MCP detector.

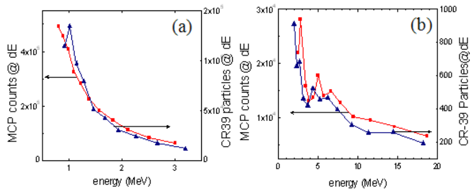

Fig.3 Correlation of integrated counts in dE energy interval due to MCP signal with number of particles on CR-39 in dE energy interval plotted with respect to energy for (a) Protons and (b) Carbons. The dE energy interval corresponds to thickness of the stripe on CCD and CR-39

3. Theoretical Model

In general the response of the MCP to the incident ion can be given as a function of channel bias angle, open area ratio, incident angle of the ions on channel, their energy and the penetration depth into the channel. All these parameters some how affect the secondary electron yield due to the ion impact and therefore the gain of the MCP channel. Following Beuhler and Friedman [6] a general expression for the secondary yield from a solid target can be given by

$$\gamma_a = \frac{P}{E_0} \int_0^{\infty} e^{-\frac{x\cos\theta}{\lambda}} \left(\frac{dE}{dx}\right)_e dx \tag{1}$$

where P is the probability of electron escape from the surface, E_0 is the energy (eV) needed to be deposited to produce an electron for escape, λ is the characteristic length of electron diffusion inside the target, $(dE/dx)_e$ is the electronic stopping power of the projectile ion into the target and θ is the angle of incidence with respect to the normal to the target surface [7]. Several investigations have shown experimentally [8] and by numerical simulations [9] the dependence of secondary yield γ_a on the electronic stopping power of the projectile ion $(dE/dx)_e$ over a broad range of ion energies. In addition, the angular dependence of the secondary yield $\gamma_a \propto 1/\cos\theta$ was shown experimentally by Thieberger et al [10] for carbon ions. In our model calculations we have considered the same dependences. Assuming in (1) that P, E_0 and λ are constant for a particular material and $(dE/dx)_e$ can be considered constant as well for the electron escape from a very thin layer at the surface of the material, Eq.(1) becomes

$$\bar{\gamma}_a = \frac{P}{E_0} \frac{\lambda}{\cos\theta} \left(\frac{dE}{dx}\right)_e \tag{2}$$

The gain of the MCP channel is normally given as $g = e^{G.a}$, where G is the secondary emission characteristics parameter and a=L/D, where L is the channel length and D is the channel diameter [11].

Implicitly the gain depends on the voltage across the channel and a linear dependence of the voltage on channel length could be considered. In this way the gain has been calculated to be, $g = e^{k.(L - z_{pd})/L}$, where Z_{pd}, is the penetration depth and k is constant. In our case, since the MCP is installed in a Thomson spectrometer, and therefore the angle of incidence of the dispersed ions on the MCP differs for different energies, the penetration depth Z_{pd} is also different, and therefore the gain will be in principle different. A Monte-Carlo simulation has been therefore performed in order to obtain the most probable penetration depth and consequently the gain in the channel. We have considered the intersection of straight line ion trajectories with cylindrical channels whose direction cosines incorporate ethe incidence angle and channel bias angle. Finally the response of the MCP can be written as

$$\text{Response}_{\text{MCP}} \propto \frac{1}{\cos\theta} \cdot \left(\frac{dE}{dx}\right)_e \cdot \text{g} \tag{3}$$

To obtain $(dE/dx)_e$ for different energy ions we used the SRIM [12] program and the angle of incidence defined by the geometry of the experiment. For C^{6+} ions θ was ~82^0 at 6 MeV and ~89^0 at 240 MeV and for protons θ was ~82^0 at 0.8 MeV and 87^0 at 5 MeV. As discussed above, in calculating the 1/cosθ dependence, we take into account that the incidence angle θ with respect to the normal to the MCP channel surface varies for different ion energies in the spectrometer. The model provides a good agreement to our data except for the lower energy proton range (below 1.5 MeV). The experimental calibration data at higher energy range is shown in Fig. 4(a) and (b) together with the model calculation for the response of the MCP. We see in Fig. 4(b) a good agreement for carbon ions and a change in response by a factor of 1.5 passing from 20 to 240 MeV. However there is a disagreement for the lower energy protons (<1.5 MeV) between the theory and experimental data shown in Fig. 4(a) which we are currently investigating. We note that the relative error in this part of the spectrum is higher (about 20%) due to the higher percentage error in determining the energy range.

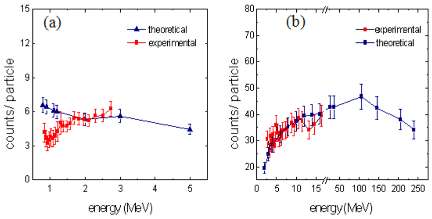

Fig.4 Response of MCP (counts/ particle) (a) for Protons and (b) for C^{6+}

4. Conclusions

In conclusion, in this paper we have described the measured particle response of an MCP detector employed within a Thomson spectrometer. The calibration delivers the relation between a registered count numbers in the CCD image of the phosphor screen which results from ion impact. The particle response of the whole detection system was evaluated by using a laser accelerated ion beam containing protons up to 3MeV and carbon ions up to 16 MeV energies. Based on a model for the MCP response the calibrations have been extended to higher energies range. The data analysis has highlighted the dependence of MCP response on incident ion species. This sensitive detection set-up makes it possible to measure on a single shot basis the ion spectrum in absolute terms.

Acknowledgements

This work was supported by EPSRC grants EP/E035728/1 (LIBRA Consortium) and EP/F021968/1. We acknowledge the support of the CLF staff at RAL.

References

[1] R. Snavely, et al., Phys. Rev. Lett. 85 (2000) 2945.

[2] E. L Clark, et al., Phys. Rev. Lett. 84 (2000) 670.

[3] M. Borghesi, et al., Fusion Sci. Technol. 49(2006)307.

[4] S. Ter-Avetisyan, M. Schnu¨rer, P. V. Nickles, J. Phys. D: Appl. Phys. 38 (2005) 865.

[5] F. H Seguin, et al.,Rev. Sci. Instrum.74 (2003) 975.

[6] R. J. Beuhler, L. Friedman, J. Appl. Phys. 48 (1977) 3928.

[7] E. J. Sternglass, Phys. Rev. 108 (1957) 1.

[8] F. J. Frischkorn, K. O. Groeneveld, Phys. Scripta T6 (1983) 89.

[9] P. H. Soltz, et al., Phys. Rev ST-Accelerators and Particle Beams 6 (2003) 054701.

[10] P. Thieberger, et al., Phys. Rev. A61 (2000) 042901.

[11] http://www.hamamatsu.com.

[12] http://www.srim.org.

Proton/ion energy scaling and laser conversion efficiency using 50fs, 10^{20}-10^{21} W/cm^2 Astra-Gemini pulses

Contacts: rprasad01@qub.ac.uk

R. Prasad, S. Ter- Avetisyan, D. Doria, K.E. Quinn, L. Romagnani, M. Zepf, and M. Borghesi
School of Mathematics and Physics, Queen's University Belfast, Belfast, UK
D.C. Carroll, O. Tresca, P. McKenna
SUPA, Department of Physics, University of Strathclyde, Glasgow, UK

C.M. Brenner, P.S. Foster, P. Gallegos, J.S. Green, A. P. L. Robinson, D. Neely
CLF, Rutherford Appleton Laboratory, STFC, Oxfordshire, UK

N. Dover, C.A.J. Palmer, M.J.V. Streeter J. Schreiber, Z. Najmudin
The Blackett Laboratory, Imperial College, London, UK

Introduction

The laser acceleration of ions to multi-MeV energies from thin foils has been investigated extensively during the last decade using intense laser pulses (10^{18} – 10^{20} W/cm^2) [1]. The ions are mainly accelerated in the space-charge fields created by laser generated relativistic electrons which are penetrating the target (e.g. Target Normal Sheath Acceleration – TNSA mechanism [2-5]). Experimental results have shown that these ions have unique properties: high brightness (about 10^{13} protons/ions per shot), high current (in kilo-Ampere range), ultralow emittance, and short pulse duration (less than 1ps), opening prospects for a broad range of applications [1]. While they have been applied successfully in high resolution radiography [6], most potential applications are demanding further improvement of the beam specifications particularly regarding maximum ion energy and ion flux .

Currently the highest proton energies (~60 MeV) and conversion efficiencies (8%) have been obtained using Nd:Glass PW systems providing 100s J, ~ ps (or several 100s fs) pulses. These systems are large-scale, costly installations, with very low repetition rate. The use of smaller scale (possibly table-top), high-rep systems is clearly preferable in view of widespread applications. For example, Ti:Sa systems reach high intensities by concentrating more moderate amounts of energies in very short pulses (10s of fs). Technological progress in this area is fast and is now enabling access to unprecedented intensities (above 10^{20} W/cm^2), with ultrashort (~50 fs) laser pulses [7]. The interaction at these intensities still has to be explored carefully and experiments aiming to obtain scaling laws or estimates of the efficiency of the acceleration process are essential. The scaling of proton energy using ~ 50 fs lasers at intensities ranging from ~ 10^{18} to 10^{19} W/cm^2 has been reviewed in [8, 9]. Generally, acceleration with shorter pulses is, at comparable intensities, less efficient than with ps pulses. By optimizing target thickness (down to tens of nm) [8, 10, 11], maximum conversion efficiencies into protons of about 1 % have been inferred.

Additionally, PIC simulations using circularly polarised light and intensity >10^{20} W/cm^2, have shown a transition from the usual TNSA process to a regime of radiation pressure acceleration (RPA) [12, 13]. The advantage of using circularly polarised pulses lies in the fact that the oscillating components of the Lorentz force in the direction perpendicular to the sharp density gradient is quenched, and hence the motion of the electrons at the interaction surface is mostly adiabatic and electron heating is strongly reduced [12]. The ions are accelerated via space charge fields which balance the radiation pressure (i.e. the ponderomotive force).

In this report we will discuss the effect of the laser polarisations, target thickness and target material on the energy of the accelerated protons/ions under normal laser incidence on the target. Also we will discuss the total number of protons/carbon ions produced during the interaction at two different laser incidence angles namely 35^0 and 0^0 for a range of target thickness.

Experimental Method

The experiments have been carried out on ASTRA-Gemini laser at Rutherford Appleton Laboratory, which delivers 12 J ultra-short (~50 fs) pulses at a central wavelength of 800 nm. The intrinsic intensity contrast of 10^7 at 20 ps prior to the pulse peak was enhanced to the level of ~10^{10} employing a “double plasma mirror” system, which preserves the spatial focal spot qualities although the throughput laser energy is reduced to ~6J. An f/2 off axis parabola was used to focus the laser pulses to a spot size of diameter ~2.5 μm containing 35% of laser energy. Thus, intensities above 5×10^{20} W/cm^2 could be reached. Al and carbon targets with thickness varying from 10 nm up to 10 μm were irradiated up to this intensity. Thomson spectrometers with absolutely calibrated micro-channel-plate (MCP) detectors registered ion emission spectra simultaneously along different directions: along the laser propagation axis

(0^0), and at angles of 35^0, 45^0 and 215^0 relative to the laser axis. The spectrometers employed 100 µm-diameter entrance pinholes located at a distance of 130, 93, 95 and 81 cm from the target surface, respectively. The schematic of the experimental set up has been shown in fig1.

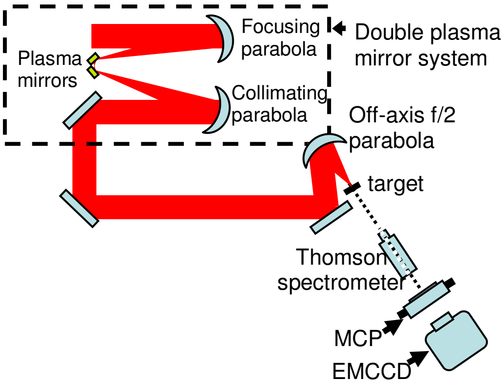

Fig.1 Experimental setup: A double plasma mirror was employed to enhance the laser pulse contrast.

Results and Discussion

The dependence of the maximum proton energy on carbon target thickness at two different polarisations viz. linear and circular at normal incidence is shown in fig 2(a).

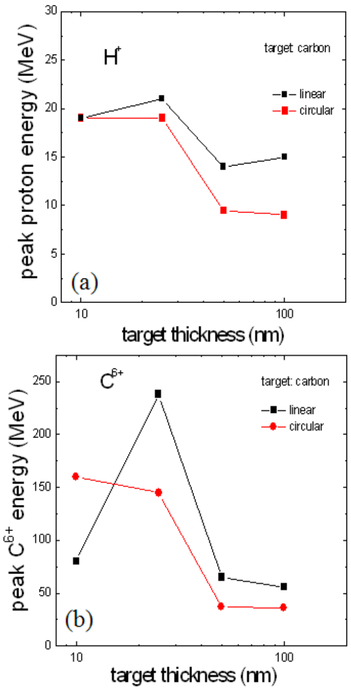

Fig.2 Maximum proton/ion energy dependence on target thickness at normal incidence on carbon target for linear and circular polarisations

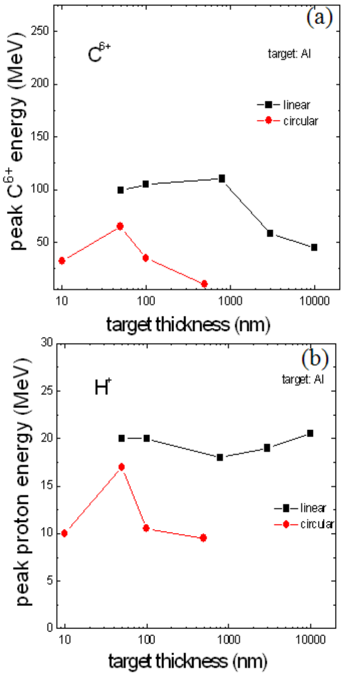

Fig.3 Maximum proton/ion energy dependence on target thickness at normal incidence on aluminium target for linear and circular polarisations

Proton energy increases with decrease in target thickness for both polarisations and there is factor of 2 gain in energy (~20 MeV) at 25nm compared to 50nm for the circular polarization case (~1.5 times gain in linear case).

Similarly in fig2(b) we have shown the carbon ions energies dependence on thickness for two polarisations. At circular polarisation, the C^{6+} energy increases with decrease in thickness and is ~160 MeV at 10 nm with a ~ 4 times increase in energy going from 100nm to 10nm. With linear polarisation, energy increases with a decrease in thickness up to 25 nm reaching ~240 MeV.

Next, we investigated the dependence of proton/ion energy on the target thickness but now with aluminium target at normal incidence. In fig3(a) the proton energy dependence on thickness at circular and linear polarisation is shown. Similar to the case of fig 2, for circularly polarized light the proton energy increases with decrease in thickness. Surprisingly for linear polarisation we see an almost constant maximum energy ~20 MeV at all thicknesses ranging from 10um to 50nm. On the other hand in fig 3(b) C^{6+} energy has been plotted with target thickness. For both polarisations we see an increase in the energy as thickness decreases.

The dependence of produced number of protons/ions at two different laser incidence angles 35^0 and 0^0 on the target as a function of target thickness for the aluminium target has also been investigated. In fig.4(a) the total number of protons and carbons detected along the rear surface target normal (RSTN) within a solid angle of 9 nsr (hereafter we will label this quantity as proton/ion flux) has been plotted against target thickness under 35^0 laser incidence. The proton/ion flux increases with decrease in thickness up to 100nm and decreases below this thickness. The numbers are integrated over the 2 - 12 MeV range for protons and 2.5 - 42 MeV for Carbon ions. Both, proton and ion flux increased by an order of magnitude when the target thickness was decreased about 200 times. One can try to estimate the conversion efficiency into protons for 100 nm thick targets by assuming a proton beam divergence of about 8^0 (as suggested by other diagnostics) which gives ~ 6.5% (~ 5% for carbon ions).

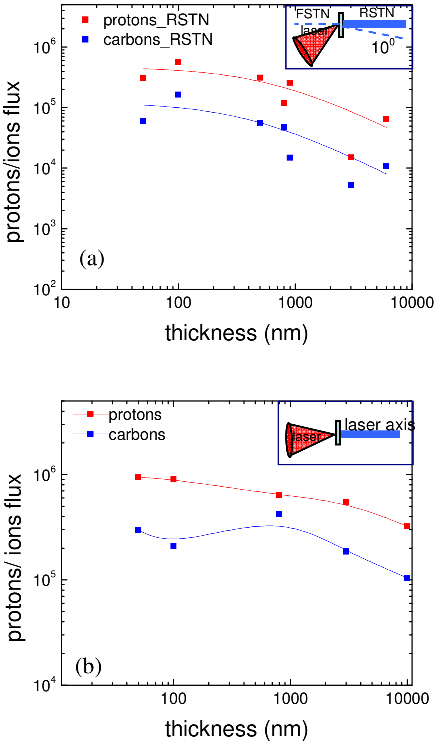

Fig.4 Number of accelerated protons and carbon ions as a function of target (Al) thickness (a) Along rear surface target normal (b) along laser axis forward direction

Conclusion

In summary we have presented the energy scaling for protons and carbon ions as a function of target thickness for two different target material (Al, C) and two different polarisations (linear and circular). Also the dependence of produced proton/ion flux was shown for two incidence angles namely 35^0 and 0^0. The interpretation and modelling of this data is currently ongoing.

Acknowledgements:

This work was funded by EPSRC grants EP/E035728/1(LIBRA consortium), EP/F021968/1 and EP/C003586/1, and by STFC Facility access. We acknowledge the support and contribution of the Target Preparation Laboratory, ASTRA laser staff and the Engineering workshop at CLF, RAL.

References:

1. M. Borghesi *et al.,* Fusion Science and Technology, 49 (2006) 307
2. R. Snavely *et al.,* Phys. Rev Lett., 85 (2000) 2945
3. E. L Clark *et al.,* Phys. Rev. Lett. 84 (2000) 670
4. A. Maksimchuk, S. Gu, K. Flippo, and D. Umstadter, Phys. Rev. Lett. **84**, 4108 2000)
5. S Hatchett et al., Phys. Plasma 7 (2000) 2076
6. M. Borghesi et al., Phys. Plasmas 9, 2214 (2002)
7. http://www.clf.rl.ac.uk/Facilities/Astra/Astra+Gemini/12258.aspx
8. J. Fuchs et al., Nature Physics 2 (2006) 48
9. L. Robson, et al., Nature Phys. 3, 58 (2006),
10. D Neely et al., Appl. Phys. Lett. 89 (2006) 021502
11. I Spencer et al., Phys. Rev. E 67 (2003) 046402
12. A. Macchi *et al.,* Phys. Rev. Lett . 94 (2005) 165003
13. A. P. L. Robinson *et al.,* New J. Phys. 10 (2008) 013021

Investigation of Contrast of Astra/Gemini

Y. Tang, C. J. Hooker, O. V. Chekhlov, S. Hawkes, K. Ertel and R. Pattathil

Central Laser Facility,
STFC Rutherford Appleton Laboratory, Chilton, Oxon OX11 0QX, UK

Main contact email address: *yunxin.tang@stfc.ac.uk*

Introduction

With remarkable progress in chirped pulse amplification (CPA) technology, extreme laser power and intensity as high as 10^{22}W/cm^2 has recently been made available by the new generation femtosecond (fs) petawatt (PW) Ti:Sapphire amplifiers [1-4]. Such ultrahigh intensities have opened a way to the experiments in the ultra-relativistic and radiation dominated regime of laser-matter interaction [5-6]. The temporal contrast of the laser pulse, defined as the ratio of the peak intensity of the pulse to the prepulse intensity, plays a crucial and important role in the ultra high field laser-matter interaction experiments. It generally requires a clean laser pulse with a contrast better than 10^{10} to restrict any destructive preplasma dynamics in those experiments, as excessive prepulse intensity can significantly modify the solid targets and experiment conditions due to preplasma formation prior to the arrival of the main pulse.

There are two major types of prepulses in the temporal profile of ultrafast, high power laser pulses: the incoherent and coherent pedestals. The first is normally caused by the amplified spontaneous emission (ASE) on the ns time scale while the second, on the order of tens of ps time scale, is related to the residual high order spectral phase, spectral phase noise, random spectral modulation and degree of non-Gaussian shape introduced through the CPA laser system. The incoherent ASE contrast is generally considered to be more detrimental than the coherent contrast as it is on the relatively long ns time scale which could result in sufficient preplasma expansion to alter the experimental conditions significantly [7-8]. To meet an increasing demand for higher temporal quality of the laser pulse by considerably reducing both the incoherent and coherent noise level has posed a big challenge to the development of extreme power laser systems.

In this article, we have report an investigation of the temporal contrast of the Astra-Gemini high power Ti:Sapphire laser. Enhanced contrast of the laser pulse by nearly an order of magnitude has been achieved by upgrading the commercial front-end to provide cleaner seed pulses.

Results and discussion

Astra-Gemini, as a world leading PW high power solid-state laser facility, has been in operation successfully for more than two years. The Astra laser is a well established high power Ti:Sapphire system based on CPA technology. This laser system consists of a commercial front-end including a Ti:Sapphire mode-locked oscillator and a 9-pass Ti:Sapphire amplifier (Femtolaser) operated at 1kHz; a grating pulse stretcher; a chain of three multi-pass Ti:Sapphire amplifiers working at a repetition rate of 10Hz and final recompression by a pair of gratings. Pulses of duration ~45fs at energies up to 0.7J was delivered at 10Hz. An acoustic-optic programmable dispersive filter (AOPDF, Dazzler) is also used in the front end to control the overall spectral bandwidth and compensate the residual high order phase. Detailed information on configurations, geometries and specifications of the Astra laser facility can be found elsewhere [3-4].

In order to improve the contrast of the laser pulse to meet the requirement for high field laser-matter interaction applications, we undertook an extensive study of temporal profile of the Astra laser pulse. Initially, the temporal profile of the pulse from the existing system was measured with a commercial third-order auto-correlator (SEQUOIA) to provide a baseline of comparison for further optimisation and improvement. A typical contrast measurement of the Astra laser pulse is shown in Figure 1.

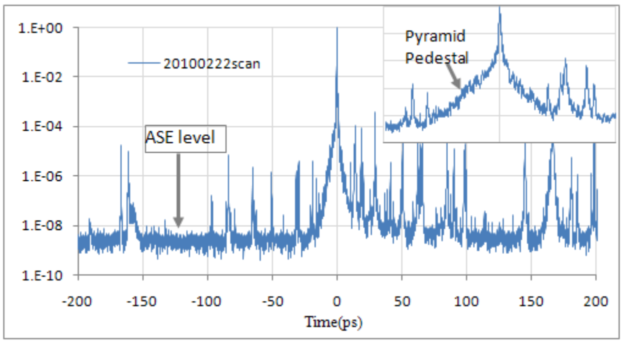

Fig.1 Typical temporal profile of the Astra pulse

As seen, the background noise level of the laser pulse on the ns timescale is in the region of ~3x10^{-9} compared with the main peak, corresponding to an incoherent ASE contrast of ~3x10^8. The pyramid shaped pedestal in the time range of ~15ps close to the main peak has a relatively high intensity up to ~3x10^{-5} with respect to the main peak, corresponding to a coherent contrast of ~3x10^4. There are also some sub-peak prepulses presented in the temporal profile, which will be discussed in the later section of this report.

For a designed intensity specification of Astra-Gemini laser at ~10^{22}W/cm^2, the incoherent ASE and coherent contrast of the existing laser system represent prepulse intensity at ~10^{13}W/cm^2 and 10^{17}W/cm^2, respectively, which well exceeds the intensity threshold for plasma formation at ~10^{10} W/cm^2. Therefore, minimising the ASE background noise level was one of the major concerns of this investigation.

Various techniques have been investigated for possible improvement in the temporal quality. Firstly, a near-diffraction limited spatial filter has been implemented between the stretcher and the first amplifier (AMP1), in conjunction with a near-field aperture, to clean up any stray light into the amplifier. The measurement showed that there was no impact on the temporal contrast by either spatial filter or near-field aperture or both. Secondly, the extinction ratio of the fast pockel cell between the front-end and the stretcher has been optimised and improved by nearly one order of magnitude by using better quality polarisers. In addition, the original gold-coated back mirror in the stretcher was replaced by a dielectric-coated one to minimise losses and scattering due to the degradation of the gold coating. Unfortunately, all these changes produced no observable impact on the contrast.

For an extreme power CPA laser system such as Astra-Gemini, the front-end provides the seed pulse for the subsequent amplifiers for further pulse energy amplification. Meanwhile the front-end has an amplification gain of $>10^6$, representing the highest gain section of the whole system. This implies that the ASE noise has been amplified the most in this section as well. Reducing the ASE noise level in the front-end system should therefore reduce the overall ASE background level of the whole system. To fulfil this task, the front-end system was upgraded by replacing the original JADE1 pump laser by a JADE2 for more reliable and stable operation. During this upgrade and system optimization, the Dazzler was relocated to a position after the first four passes of the multi-pass amplifier, and the Berek polarization compensator was removed altogether. The effect of these changes was to enhance the extinction ratio by a factor of up to 10, thereby significantly suppressing the intracavity ASE and enhancing the temporal contrast.

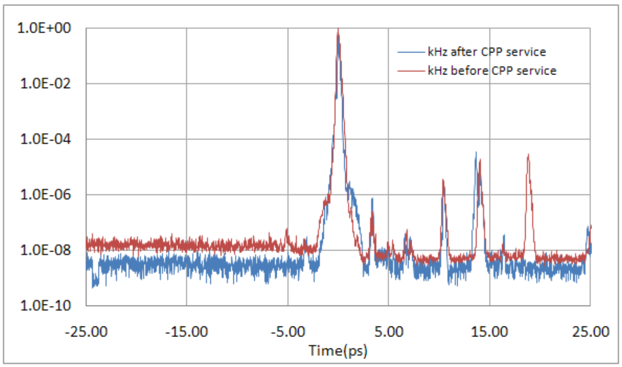

Fig.2 Front-end Contrast before and after upgrading

The output pulse from the front-end was directly recompressed to near transform limit by a prism compressor and the temporal contrast was measured with the Sequoia. Figure 2 shows the contrast measurement of the front-end before and after upgrading. It is clear that the ASE contrast has been improved by almost one order of magnitude. The contrast of the Astra-Gemini pulse was measured again after the front-end upgrading, and the result is shown in Figure 3. It is evident that the overall incoherent and coherent contrast of the Astra-Gemini laser pulse was enhanced by nearly one order of magnitude due to cleaner seed pulses delivered from the upgraded front-end.

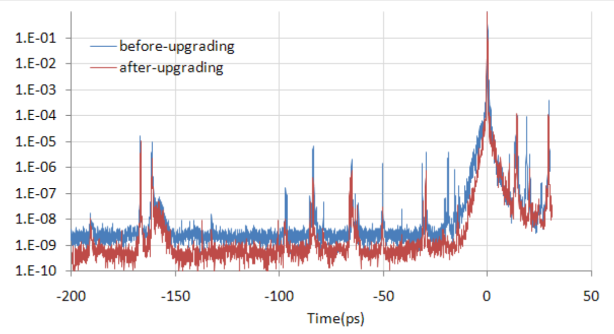

Fig.3 Overall contrast before and after front-end upgrading

As mentioned before and seen in Fig.1, there are a number of sub-peak prepulses appearing in the time range of up to ~200ps prior to the main pulse. Unlike the incoherent and coherent pedestal prepulse, the sub-peak prepulses are replicas of the main pulse at much reduced intensity. They are much shorter than the ASE and coherent pedestals discussed above. The replica prepulses are usually generated by internal multiple reflections in various optical components, such as windows, lenses, polarisers and Ti:sapphire crystals, throughout the laser system. It is well-known that the post-pulse at a certain temporal displacement with respect to the main pulse is generated at much reduced intensity by the internal Fresnel reflections even when the surfaces have antireflection coatings. The stretched, chirped post-pulse with a time separation from the main pulse less than the stretched pulse duration will be coupled with the chirped main pulse, producing both temporal and spectral modulation by interference. Any non-linear distortion of this modulation by high B-integral will generate new satellites after recompression. As a result, a counterpart prepulse of the post-pulse will appear before the main pulse when the pulse is compressed. The intensity of this prepulse is given by $\sim 0.6B^2$ W, where B is the B-integral of the main pulse and W the intensity of the post-pulse [9]. Similar prepulses appear in contrast traces of many CPA systems, and are frequently (and wrongly) dismissed as artefacts of the measurement.

The replica prepulse can also affect the high field laser-matter interaction experiment dramatically by preheating or pre-ionizing the solid targets, and ideally should be suppressed and ultimately eliminated. To provide a cleaner and higher temporal quality pulse, a number of components in Astra with broadband antireflection coatings were replaced by optics having V-coatings, which typically have reflectivities of 0.1 to 0.2%, compared with around 1% for broadband coatings. By making these substitutions, some of the replica post-pulses and their counterpart pre-pulses were reduced by a factor of ~100, as shown in Figure 4.

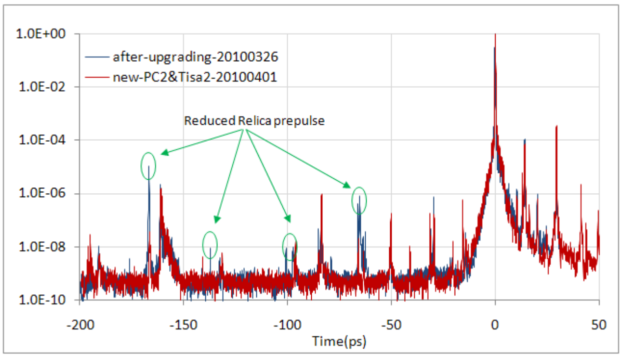

Fig.4 Replica pre-pulse reduction in the temporal profile

Conclusions

The temporal profile of Astra-Gemini laser pulse was extensively investigated under various conditions. The background contrast of the laser pulse was enhanced by nearly an order of magnitude by upgrading and optimizing the commercial front-end to provide a cleaner seed pulse. Some of the replica pre-pulses were reduced or eliminated by the use of components with better quality antireflection coatings.

References

1. S.-W. Bahk, P. Rousseau, T. Planchon, V. Chvykov, G. Kalintchenko, A. Maksimchuk, G. A. Mourou, and V. Yanovsky, Opt. Lett. **29**, 2837 (2004).
2. G.A. Mourou, T. Tajima, S.V. Bulanov, Rev. Mod. Phys. **78**, 309 (2006).
3. C. Hooker *et al*, CELO/QELS 2008, JThB2, (San Jose, CA, USA, May 4-9 2008)
4. Klaus Ertel et al., *'ASE suppression in a high energy Titanium Sapphire amplifier'*, Opt. Express **16,** 8039 (2008)
5. D. Umstadter, Phys. Plasma **4,** 1774 (2001).
6. A. Zhidkov, J. Koga, A. Sasaki and M. Uesaka, Phys. Rev. Lett. **88,** 185002 (2002).
7. V. Chvykov, P. Rousseau, S. Reed, G. Kalintchenko and V. Yanovsky, Opt. Lett. **31,** 1456 (2006).
8. L. Antonucci, J. P. Rousseau, A. Jullien, B. Mercier, V. Laude and G. Cheriaux, Opt. Comm. **282,** 1374 (2009).

9. N. V. Didenko, A. V. Konyashchenko, A.P. Lutsenko, S. Yu. Tenyakov, Opt. Express **16,** 3178 (2008).